Transition Waves and Formation of Domain Walls in Multistable Mechanical Metamaterials

H. Yasuda, L. M. Korpas, and J. R. Raney*
Department of Mechanical Engineering and Applied Mechanics, University of Pennsylvania, Philadelphia, Pennsylvania 19104, USA

(Received 9 January 2020; revised manuscript received 19 March 2020; accepted 30 March 2020; published 27 May 2020)

We experimentally, numerically, and analytically investigate transition waves in a mechanical metamaterial comprising a chain of tristable elements. Transition waves can be initiated from different stable phases within the highly tunable tristable energy landscape. These waves propagate via coupled translational and rotational motion that leads to formation of stationary domain walls if transition waves of incompatible type collide. Since domain formation and propagation is fully reversible, the unique nonlinear behavior could be exploited in new classes of reconfigurable metamaterials.

DOI: 10.1103/PhysRevApplied.13.054067

The study of phase transformations has led to a rich theoretical understanding of the physics of materials, and to ubiquitous technological advances of critical industrial importance in metallurgy, semiconductor purification, and polymer processing [1,2]. However, the physical insight achieved along the way is not limited to traditional materials. In fact, macroscopic mechanical systems can exhibit analogous phase transitions between distinct energy minima [3–11]. Because the properties of the different phases can vary drastically [6,12], the ability to harness these transitions and their propagation in multistable systems could lead to a new class of reconfigurable metamaterials with new capabilities in diverse applications, including energy absorption [6], soft robotics [13], autonomous systems [14], and deployable structures [15,16].

Early work in understanding the propagation of phase boundaries (i.e., topological defects) in mechanical systems has focused on systems of bistable elements [11,17–22]. In these examples, the potential energy landscape is asymmetric with one minimum (phase) at a higher energy level than the other, which determines the propagation direction and speed without dependence on the form of the initial input condition [17,22]. The ability to tailor the energy landscape is therefore an important means for controlling the characteristics of the transition waves. However, when a transition wave propagates in one-dimensional (1D) bistable lattices, the entire structure becomes the same phase unless defects or heterogeneities are present [7,11,22]. If the individual elements are instead multistable, the mechanical system can both support the propagation of transition waves and, like real materials, allow the existence of multiple domains of different phases, separated by stationary domain walls (SDWs) (i.e., static boundaries between phases). In addition to their utility as material models, these systems also have potential for use as reconfigurable devices, as the combinations of distinct phases in one system could be used to tune the mechanical properties.

Here, we study a 1D chain of tristable elements composed of rotating squares with embedded magnets [Fig. 1(a)]. We experimentally, numerically, and analytically characterize the static and dynamic behavior of this system. Adjacent squares are connected at their vertices by flexible hinges, and permanent magnets are embedded [23–25] in the faces of the squares to produce attraction between the proximal faces in adjoining squares [see Fig. 1(b)], which enables reconfigurability [9,26–28] and rich static and dynamic behavior. This system exhibits coupling behavior between translational and rotational degrees of freedom (DOF), unlike previous lattices of bistable elements [17,20,22,29]. This additional DOF in each element in the chain provides more design freedom, enabling a highly tailorable tristable energy landscape as well as tunable stability (monostable, bistable, and tristable behaviors), which leads to customizable transition wave propagation and formation of domain walls. We experimentally and numerically demonstrate the propagation of the transition waves in this system that arise due to the tristable elements, and provide an analytical context for these waves. Additionally, we show that transition waves of opposite rotational character can collide to form stationary domain walls that separate two distinct phases, a phenomenon that has not been observed in uniform 1D bistable lattices.

We begin by analyzing the static behavior of our system, starting with its building block composed of four

*raney@seas.upenn.edu

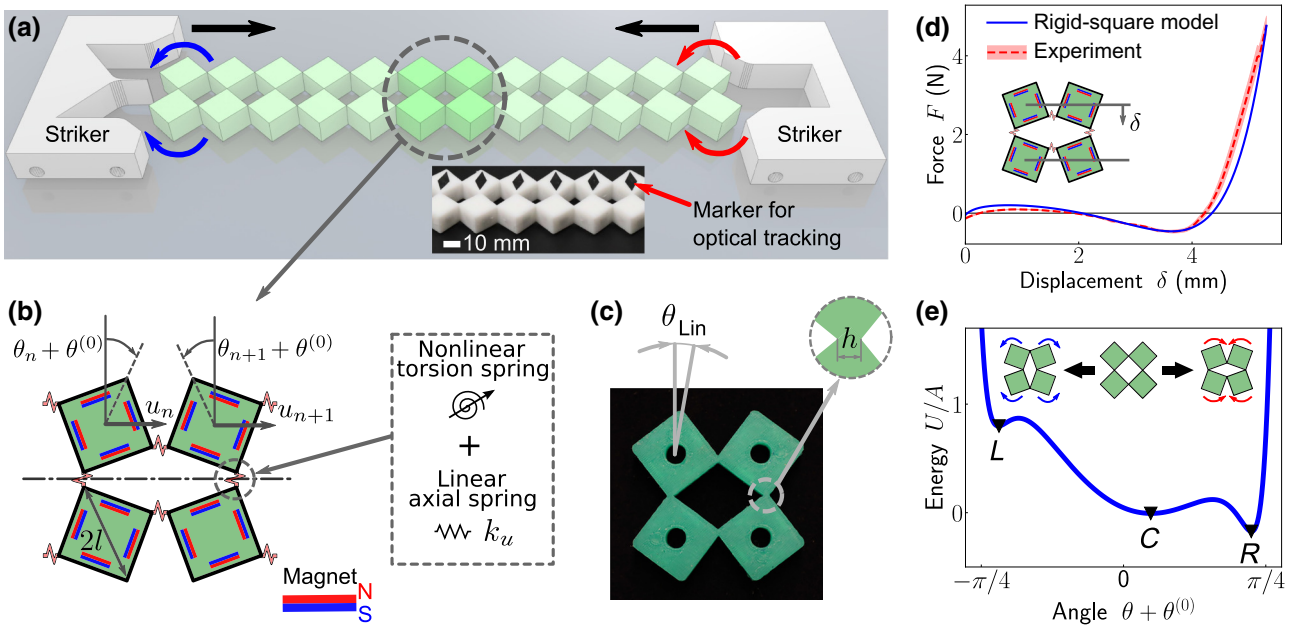

FIG. 1. (a) Conceptual illustration of a 1D chain of the rotating-squares structure. The inset photograph shows a physical prototype. (b) Schematic illustration of the building block of four squares. (c) Physical prototype made of a silicone elastomer, photographed prior to magnet insertion to illustrate θ_{Lin}. (d) Force-displacement relationship for the building block shown in (c), with hinge thickness $h = 1$ mm and $\theta_{\text{Lin}} = 8^\circ$. The dashed red curve represents the experimental mean and standard deviation, and the solid blue curve denotes the rigid-square model. This model leads to the energy landscape as shown in (e). The black triangle markers in (e) indicate three different stable phases (energy minima).

squares by modeling the system as rigid squares that are connected by axial and torsional spring elements at each vertex [Fig. 1(b)]. The motion of the squares in the nth column can be expressed by two DOFs, a displacement u_n and a change in rotational angle θ_n relative to the initial equilibrium angle $\theta^{(0)}$. The interaction between neighboring squares is modeled as a linear axial spring (with spring constant k_u) and a nonlinear torsional spring, representing stretching and bending, respectively. The torsional spring is a composite spring that includes a linear torsional spring (with spring constant k_θ and rest angle θ_{Lin}) associated with the elastomeric hinges, and a nonlinear torsional spring associated with the effect of the embedded magnets. Without magnets, the torsional spring would only consist of the linear component with stiffness related to the hinge thickness, h, resulting in an equilibrium angle $\theta^{(0)} = \theta_{\text{Lin}}$, defined by the angle at which the specimen is molded [see Fig. 1(c)]. The nonlinear torsional spring representing the magnets is expressed as two Morse potential functions. We employ the Morse potential functions to capture the effect of the magnets on the rotational degree of freedom. Although these functions are used empirically, they explicitly identify the additional energy minima in the energy landscape that arise due to the addition of the magnets, and also the depths of these new energy wells. Both of these play important roles in the static and dynamic responses of our system. We later discuss the validation of this empirical model. The expression for the potential energy of each hinge can then be written:

$$U(\Delta\theta) = \frac{1}{2}k_u|\Delta\mathbf{l}|^2 + \frac{1}{2}k_\theta(\Delta\theta)^2 + V_{\text{Morse}}(\Delta\theta), \quad (1)$$

where $\Delta\mathbf{l}$ is the deformation of the linear axial spring, $\Delta\theta = 2(\theta + \theta^{(0)} - \theta_{\text{Lin}})$, and

$$\begin{aligned} V_{\text{Morse}}(\Delta\theta) &= A\left[e^{2\alpha(\Delta\theta+2\theta_{\text{Lin}}-2\theta_{\text{Morse}})} - 2e^{\alpha(\Delta\theta+2\theta_{\text{Lin}}-2\theta_{\text{Morse}})}\right] \\ &\quad + A\left[e^{-2\alpha(\Delta\theta+2\theta_{\text{Lin}}-2\theta_{\text{Morse}})} - 2e^{-\alpha(\Delta\theta_n+2\theta_{\text{Lin}}-2\theta_{\text{Morse}})}\right]. \end{aligned} \quad (2)$$

Here, A and α are parameters that alter the depth and width of the potential, respectively, and θ_{Morse} is a parameter that alters the equilibrium points. These parameters are obtained experimentally. By using this energy expression and the principle of virtual work, we obtain the quasistatic force-displacement relationship for the four-square building block (see Note 1 within the Supplemental Material for more details [30]):

$$\begin{aligned} F = \frac{8}{L\sin(\theta+\theta_{\text{Lin}})} &\times \left\{k_\theta\theta + \alpha A\left[e^{4\alpha(\theta+\theta_{\text{Lin}}-\theta_{\text{Morse}})} - e^{2\alpha(\theta+\theta_{\text{Lin}}-\theta_{\text{Morse}})}\right]\right. \\ &\left. - \alpha A\left[e^{-4\alpha(\theta+\theta_{\text{Lin}}+\theta_{\text{Morse}})} - e^{-2\alpha(\theta+\theta_{\text{Lin}}+\theta_{\text{Morse}})}\right]\right\}. \end{aligned} \quad (3)$$

To experimentally verify this model, we fabricate the building block of Fig. 1(c) from silicone elastomers and insert magnets in the sides of each square (see Note 2 within the Supplemental Material for details [30]). We apply quasistatic displacement to the centers of two adjacent squares in the four-square unit structure (while rotation and transverse displacement remain unconstrained) and measure the force (see Note 3 within the Supplemental Material for details [30]). Figure 1(d) shows the experimental force-displacement curve for $(h, \theta_{\mathrm{Lin}}) = (1\ \mathrm{mm}, 8^\circ)$, along with the analytical prediction from the rigid-square model, demonstrating good agreement. This rigid-square model allows construction of the energy landscape as expressed in Eq. (1), with the parameters obtained experimentally (see Note 3 within the Supplemental Material [30]). Figure 1(e) shows the energy landscape (U/A) for these parameters. The structure clearly exhibits three local energy minima corresponding to three distinct stable configurations of the structure.

While tristability is one possible outcome in this system, bistability or monostability are also possible. To systematically characterize this tunability, we use the validated model to analyze the potential energy in the design space $(h, \theta_{\mathrm{Lin}})$. We refer to each energy minimum in the energy landscape as a distinct "phase" [e.g., the three phases in a tristable landscape are "L", "C", and "R", as shown in Fig. 1(e)]. Figure 2 shows a geometric phase diagram that maps the design space $(h, \theta_{\mathrm{Lin}})$ to the allowed phases. (Note the close resemblance of the phase diagram to a ternary phase diagram in classical materials [31].) If we increase h from $(h, \theta_{\mathrm{Lin}}) = (1\ \mathrm{mm}, 8^\circ)$, the tristable system would eventually become bistable [see inset (i) in Fig. 2, corresponding to $h = 1.4$ mm], or even monostable [see point (ii), corresponding to $h = 1.7$ mm]. Point (iii) indicates another bistable $(L + R)$ region. For further experimental verification of these distinct transitions, see Fig. S6 and Video S1 within the Supplemental Material [30].

Not only can the number of stable configurations be varied, but the depths of the wells and the energy barriers between them can be tuned over a large range. For example, to characterize the possible energy landscapes within the tristable phase region, we introduce the energy ratio $\xi = (\Delta U_{CL} - \Delta U_{CR})/(\Delta U_{CL} + \Delta U_{CR})$, where $\Delta U_{CL} = U_C - U_L$ and $\Delta U_{CR} = U_C - U_R$ are the differences in energy between the minima of phase L (or R) and phase C, as shown in Fig. 3(a). Here, $\xi = -1$ (or 1) indicates that the local minimum for phase L (or R) has the same energy value as that of phase C. In Fig. 3(b), we plot the value of ξ throughout the tristable region [see Fig. 3(c) for the magnified plot], indicating four distinct areas bounded by the lines (dashed) along which $\xi = \pm 1$. For example,

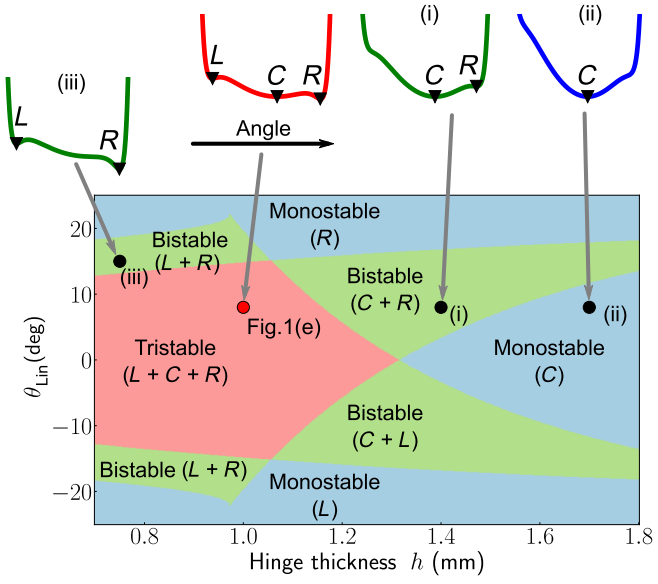

FIG. 2. Geometric phase diagram as a function of h and θ_{Lin}. The red, green, and blue regions denote tristable, bistable, and monostable configurations, respectively. The three inset plots are energy landscapes of these distinct regions, corresponding to the following configurations: (i) (1.4 mm, 8°), (ii) (1.7 mm, 8°), and (iii) $(h, \theta_{\mathrm{Lin}}) = (0.75\ \mathrm{mm}, 15^\circ)$.

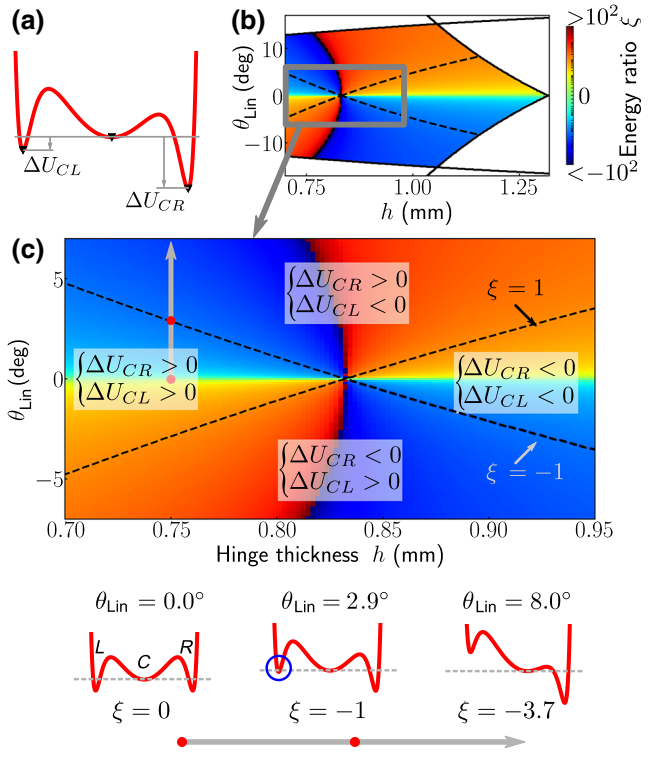

FIG. 3. (a) We analyze the tristable energy landscape by defining ΔU_{CL} and ΔU_{CR}. (b) By introducing the energy ratio (ξ), we characterize various energy landscapes within the tristable region. h and θ_{Lin} also define the energy landscape within each region, which can be varied significantly. (c) We magnify the grey box region in (b).

if we start from a symmetric potential [the lower left inset in Fig. 3(c)] and increase θ_{Lin} from 0° to 8° while holding h constant, the energy landscape becomes increasingly asymmetric. In this way, the energy landscape of the system can be tuned over a wide range, simply by controlling two parameters. Additional possible configurations are shown in Fig. S7 within the Supplemental Material [30].

This facile control of the energy landscape offers powerful control over the dynamic response, particularly the propagation of transition waves. To demonstrate this, impact tests are conducted on a 1D chain of tristable elements composed of 33 columns of squares with $h = 0.75$ mm and $\theta_{\mathrm{Lin}} = 0°$ [see Fig. 4(a) for the energy landscape]. The impact is applied to the left-most end of the chain (column $n = 1$) with a striker (see Note 4 within the Supplemental Material for more details [30]). Figure 4(b) shows three frames from the high-speed camera video. Our system exhibits coupling between rotational and translational degrees of freedom [32,33] (see Video S2 within the Supplemental Material [30]). We plot the measured rotational angle (θ_n) as a spatio-temporal surface map [see Fig. 4(c)]. We observe a distinct transition from the "open" (phase C) to a "closed" (here, phase R) state propagating from the left end of the chain to the right. Interestingly, the shape of the transition wave [as shown in Fig. 4(d) for $t = 0.1$ s] shows a shallow wave front [denoted by the blue region in Fig. 4(d)], followed by a sharp corner (at the boundary between red and blue regions).

We also use the rigid-square model to numerically characterize this scenario. Letting M_n and J_n be the mass and moment of inertia of a single square (experimentally measured to be $M_n = 1.99$ mg and $J_n = 46.6 \times 10^{-9}$ kg m^2), we derive the equations of motion for the square in the nth column (see Note 5 within the Supplemental Material for the full expression of the equations of motion [30]).

We solve these numerically using the fourth-order Runge-Kutta method. The numerical results are given by the blue markers in Fig. 4(d), showing excellent agreement with the measured wave form. We not only conduct simulations but also analyze the rotation-translation coupling behavior by employing an eigenvalue analysis (see Note 6 within the Supplemental Material [30]). We further explore the transition wave analytically and find that it can be described as a half-kink solution of a φ^6 model [34–36] (see Note 7 within the Supplemental Material [30]), in contrast with the on-site potential in the bistable lattices described by the φ^4 model [17,22,37].

Then, to examine how the shape of the energy curves influences the transition wave propagation, we perform numerical simulations of transition waves in longer chains of up to 400 columns, allowing characterization of wave velocity while avoiding the effects of reflected waves. Figure 4(e) shows the effect of θ_{Lin} on the wave velocity for $h = 0.75$ mm (neglecting damping), normalized by the velocity V_0 of the symmetric case $\theta_{\mathrm{Lin}} = 0$.

The wave speed for phase $C \rightarrow R$ transitions (red markers) increases as θ_{Lin} increases due to the decrease in the energy barrier between phase C and R as defined in Fig. S8 (within the Supplemental Material [30]) [22,38].

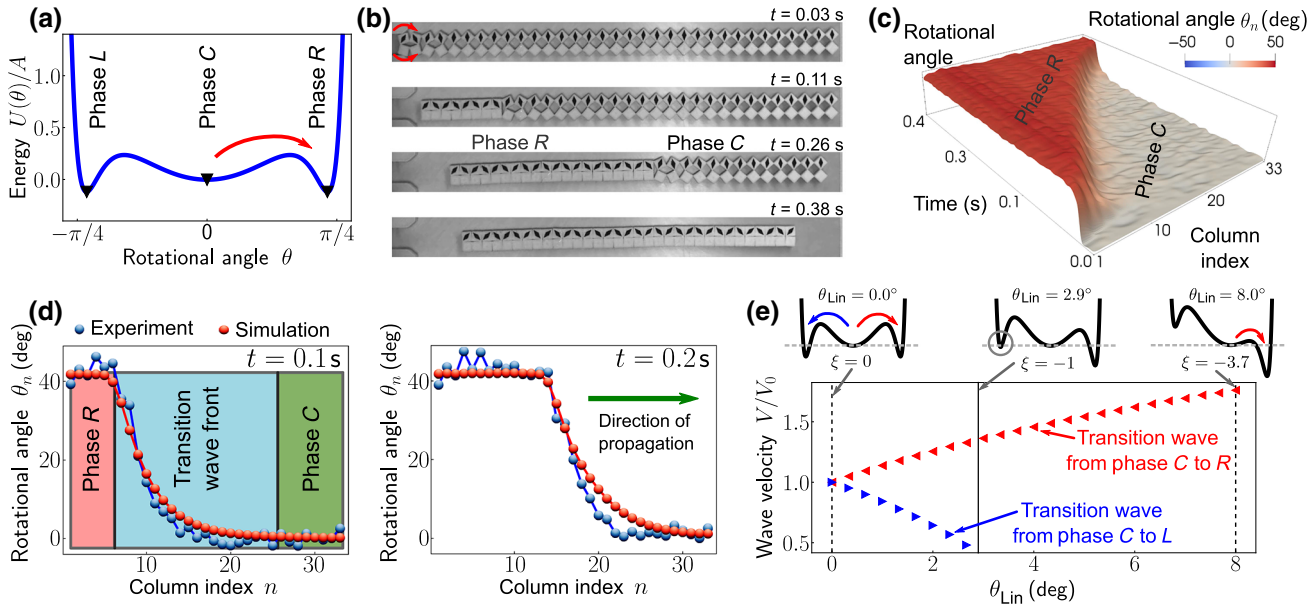

FIG. 4. (a) Tristable energy landscape used for the dynamic analysis. (b) Snapshots from experiments. (c) Surface map of rotational angle in time and space domains from the experiment. (d) Rotational angle profiles are plotted at different time frames, $t = 0.1$ s (left) and 0.2 s (right). The blue (red) markers indicate experimental (numerical) values. (e) Numerical characterization of transition wave speed during transition from phase C to phase R or phase L.

Interestingly, if $\Delta U_{CL} > 0$ and $\Delta U_{CR} > 0$, as is the case when $\theta_{\mathrm{Lin}} < 2.9^\circ$ [Fig. 3(c)], a single chain can support transition waves in both the $C \to R$ and $C \to L$ directions, each of which propagate with a different velocity (for $\theta_{\mathrm{Lin}} > 0^\circ$), a phenomenon not possible in bistable lattices.

The geometric parameters not only determine the height of the energy barriers (and thereby the wave speed), but also the energy levels of the different phases, thereby determining the allowable types of transitions among the different phases (i.e., the phase in which the transition wave begins and the phase to which the transition occurs). To demonstrate this controllability, we conduct numerical simulations of a chain composed of 400 columns (without damping) and consider two additional phase transformation patterns: $L \to C$ and $L \to C \to R$, as shown in Fig. 5. In Figs. 5(a) and 5(b), the upper and lower plots show the corresponding energy landscape and space-time evolution of the transition waves, respectively. If $(h, \theta_{\mathrm{Lin}}) = (1\ \mathrm{mm}, 0^\circ)$, the energy minima at phases L and R become higher than the minimum at phase C (i.e., $\Delta U_{CL} < 0, \Delta U_{CR} < 0$), such that propagation now requires transitions of type phase $L \to C$ or phase $R \to C$ [Fig. 5(a); see also Fig. 5(c) for snapshots from the corresponding numerical simulation]. This wave form is different from that of phase $C \to R$ propagation, with a sharp kink followed by a shallower curve. A subsequent increase in the angle θ_{Lin} to 14° enables the propagation of two sequential transition waves [38] [Fig. 5(b); see also Fig. 5(d) for the folding/unfolding behavior], which propagate with different velocities due to the difference in the energy barriers of the $L \to C$ and $C \to R$ transitions.

Finally, using the precise control of the transition wave type ($C \to R$, $C \to L$, etc.) demonstrated above, we demonstrate that our tristable system can exhibit not only traveling phase boundaries, as in bistable systems, but also stationary domain walls, which form when transition waves of contradictory type collide. Returning to the case of $(h, \theta_{\mathrm{Lin}}) = (0.75\ \mathrm{mm}, 0^\circ)$, we initiate a phase transition simultaneously at each end of the chain, one from phase $C \to L$ and the other from phase $C \to R$ [Fig. 6(a)]. Figure 6(b) shows experimentally the propagation and collision of the two different transition waves (see Video S3 within the Supplemental Material [30]). Interestingly, instead of the transition waves merging, penetrating or repelling each other, a stationary domain wall forms between phase L and phase R [Fig. 6(c)]. Note that in similar 1D chains composed of rotating elements but without the magnets, solitary waves can propagate but not transition waves. If solitary waves of opposite rotation collide they repel each other rather than forming a stationary domain wall [39]. The transition of the system

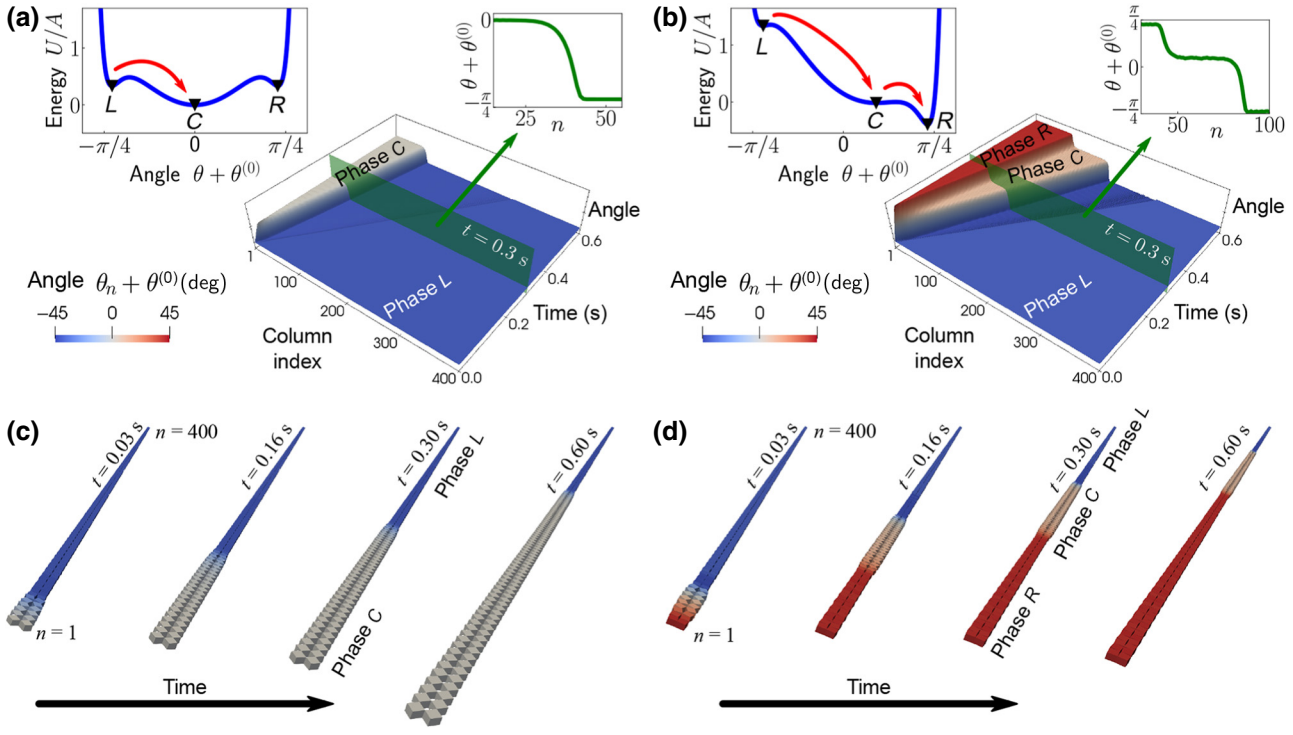

FIG. 5. Transition waves in chains with (a) (1.0 mm, 0°), and (b) (1.0 mm, 14°), each with the corresponding energy landscape (top) and surface plot for propagation of rotation (bottom). The wave form at $t = 0.3$ is shown in the inset. (c),(d) Three-dimensional (3D) reconstructions of the numerical simulations that correspond to (a),(b), respectively.

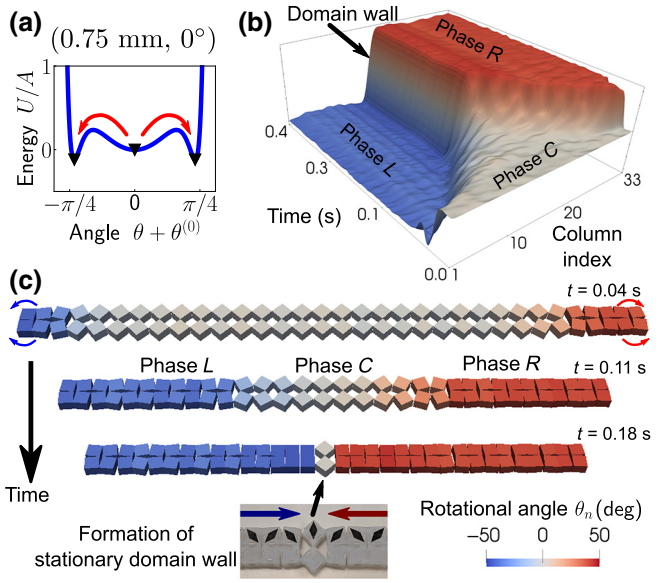

FIG. 6. Collision of transition waves with opposite rotations. (a) Tristable energy landscape with $(h, \theta_{\mathrm{Lin}}) = (0.75\ \mathrm{mm}, 0°)$. (b) Surface map of rotational angle in time and space domains shows a stationary domain wall. (c) 3D reconstruction of the experimentally measured collision behavior of the chain. The photo shows the actual domain wall created in our prototype.

from a single-phase to two phases separated by a stationary domain wall is a unique features of this system, arising from the tristable potential and the control afforded over ΔU_{CL} and ΔU_{CR}. Collisions have been studied previously by using 1D chains such as an array of pendulums [40], which can be described by the Sine-Gordon equation, but the transition waves usually pass through each other.

We now turn our attention to the effect of this stationary domain wall on mechanical properties. To examine this, we measure the static response of the chain starting from phase L without a stationary domain wall, as shown in Fig. 7(a)(i). In this experiment, we fix the position of the hinge at $n = 1$, which connects upper and lower square elements, while the rotation is not constrained. Then, we apply the tension to the right-most hinge at a constant speed of 3 mm/s (see Note 8 within the Supplemental Material for the details of our experimental setup [30]). Our test clearly shows the phase transition initiating from the right end of the chain, i.e., the loading point, and propagating to the other end (such phase transformation behavior can also be found in kirigami-based structures [41]). This eventually brings the entire chain to phase C (see Video S4 within the Supplemental Material [30]). The phase changes are fully elastic and reversible, as the material remains in the elastic regime. The structures are therefore reconfigurable, in this case with two types of phase transitions: one from a higher-energy state to a lower-energy state, and the other in the opposite direction. Figure 7(b) shows the force-displacement curve for the chain without a SDW ("no SDW"). The force curve shows a serration shape, maintaining a nearly constant force level as the chain incrementally opens.

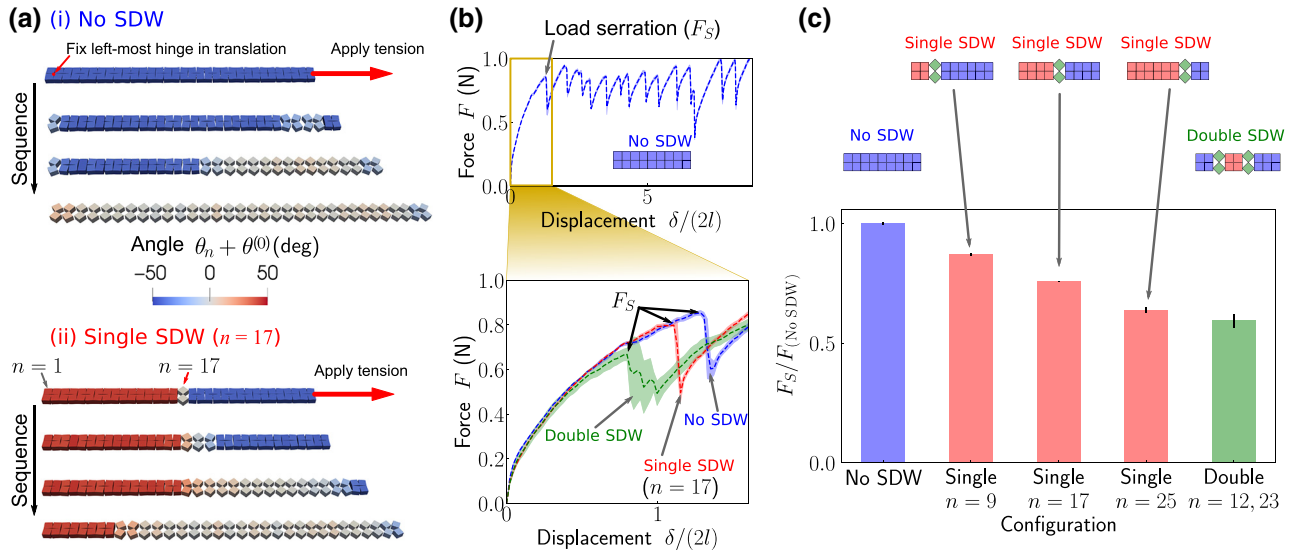

FIG. 7. Transition from phase L (or R) to a higher-energy state, phase C. (a) 3D reconstructed images of the tensile tests on a 1D chain for two different initial configurations: (i) all square elements are initially in phase L, and (ii) a single SDW is embedded at column $n = 17$, which connects the left half (phase R) and right half (phase L) of the chain. (b) A force-displacement curve obtained from the experiments is shown for the case of no domain wall. The bottom inset is the magnified view of the force plot in which single-SDW and double-SDW cases are included. (c) We experimentally measure the first peak of force [denoted by the arrow in (b) (upper)] for various configurations. The error bars indicate the standard deviation calculated from three tests on an identical sample for each configuration.

Next, we embed a single SDW into the chain manually at $n = 17$ (the center of the chain), acting as an interface between phase R on the left and phase L on the right, as shown in Fig. 7(a)(ii), and subsequently apply tension to the chain. Unlike the first case in which no SDWs are present (no SDW), the transitions begin around the SDW and propagate to the right end. Then, the interface between phase R and phase C moves to the left (see Video S5 within the Supplemental Material [30]). The lower inset of Fig. 7(b) shows the initial increase of the tensile force for both no SDW (denoted in blue) and single SDW (denoted in red). Interestingly, the point at which the force first drops [denoted by the black arrows in Fig. 7(b)] takes place at a lower force and displacement when a SDW is present (single SDW) than when it is not (no SDW). This is due to the larger average distance between magnets around the SDW and phase boundary. If we embed two SDWs in the system, this point decreases further.

To analyze the initiation of the transition motion under tension, we extract the first peak of the force (F_S) for five different configurations; no SDW (phase L), single SDW (embedded at $n = 9$, 17, or 25), and double SDW ($n = 12$ and 23). Figure 7(c) shows the different F_S values as a function of the chain configuration. As we increase the number of SDWs, F_S decreases. Also, focusing on the single-SDW case, if the location of the SDW is closer to the right end, F_S becomes smaller. This spatial dependence suggests the possibility of identifying the position of the SDWs by simply measuring F_S, without knowing the configurations of all square elements.

In summary, we experimentally, numerically, and analytically characterize a mechanical metamaterial comprising multistable (tristable) elements, and establish a framework for understanding transition wave propagation in this system. Careful control over the potential energy landscape of the individual elements is afforded by a phase diagram, which delineates the geometric parameter values at which multiple phases can coexist. We demonstrate that quasi-one-dimensional chains of tristable elements support transition waves with not only readily controlled wave speeds [22,38], but also characteristics not observed in previous work on transition waves in 1D bistable lattices, including coupled rotational and translational DOF, bidirectional and two-step propagation, and the formation of stationary domain walls upon the collision of incompatible transition wave fronts. The ability to move, reverse, and add phase boundaries raises the prospect of metamaterials that can be dynamically reconfigured based on one or two simple inputs. The incorporation of such a platform with advances in soft robotic and active material systems will pave the way towards spatiotemporal control over complex dynamic behaviors.

ACKNOWLEDGMENTS

The authors gratefully acknowledge support from the Army Research Office Grant No. W911NF-1710147I, Air Force Office of Scientific Research Award No. FA9550-19-1-0285, and from the National Science Foundation through Penn's Materials Research Science and Engineering Center (MRSEC) DMR-1720530I. L.M.K. is partially supported by a Department of Education GAANN fellowship Grant No. P200A160282I to the Department of Mechanical Engineering and Applied Mechanics at Penn. We thank Drs. Rajesh Chaunsali and Georgios Theocharis for helpful discussions, and the staff of Penn's Additive Manufacturing Laboratory for assistance with fabrication of the molds.

H.Y. and L.M.K. contributed equally to this work.

[1] F. Jona and G. Shirane, *Ferroelectric Crystals* (Pergamon Press, Oxford, UK, 1962).

[2] A. Onuki, *Phase Transition Dynamics* (Cambridge University Press, Cambridge, UK, 2002).

[3] I. Benichou and S. Givli, Structures undergoing discrete phase transformation, J. Mech. Phys. Solids **61**, 94 (2013).

[4] A. Rafsanjani, A. Akbarzadeh, and D. Pasini, Snapping mechanical metamaterials under tension, Adv. Mater. **27**, 5931 (2015).

[5] D. Restrepo, N. D. Mankame, and P. D. Zavattieri, Phase transforming cellular materials, Extreme Mech. Lett. **4**, 52 (2015).

[6] S. Shan, S. H. Kang, J. R. Raney, P. Wang, L. Fang, F. Candido, J. A. Lewis, and K. Bertoldi, Multistable architected materials for trapping elastic strain energy, Adv. Mater. **27**, 4296 (2015).

[7] M. J. Frazier and D. M. Kochmann, Atomimetic mechanical structures with nonlinear topological domain evolution kinetics, Adv. Mater. **29**, 1605800 (2017).

[8] Y. Zhang, B. Li, Q. S. Zheng, G. M. Genin, and C. Q. Chen, Programmable and robust static topological solitons in mechanical metamaterials, Nat. Commun. **10**, 5605 (2019).

[9] T. Chen, X. Zhang, X. Yan, B. Zhang, J. Jiang, S. Zhang, C. Guo, D. Huang, and M. Qi, in *Proceedings of SPIE 10968, Behavior and Mechanics of Multifunctional Materials XIII* (2019), p. 109680W.

[10] Y. Zhang, D. Restrepo, M. Velay-Lizancos, N. D. Mankame, and P. D. Zavattieri, Energy dissipation in functionally two-dimensional phase transforming cellular materials, Sci. Rep. **9**, 12581 (2019).

[11] L. Jin, R. Khajehtourian, J. Mueller, A. Rafsanjani, V. Tournat, K. Bertoldi, and D. M. Kochmann, Guided transition waves in multistable mechanical metamaterials, Proc. Natl. Acad. Sci. **117**, 2319 (2020).

[12] M. Schaeffer and M. Ruzzene, Wave propagation in reconfigurable magneto-elastic kagome lattice structures, J. Appl. Phys. **117**, 194903 (2015).

[13] T. Chen, O. R. Bilal, K. Shea, and C. Daraio, Harnessing bistability for directional propulsion of untethered, soft robots, Proc. Natl. Acad. Sci. **115**, 5698 (2017).
[14] Y. Jiang, L. M. Korpas, and J. R. Raney, Bifurcation-based embodied logic and autonomous actuation, Nat. Commun. **10**, 128 (2019).
[15] C. Liu and S. M. Felton, Transformation Dynamics in Origami, Phys. Rev. Lett. **121**, 254101 (2018).
[16] A. Zareei, B. Deng, and K. Bertoldi, Harnessing transition waves to realize deployable structures, Proc. Natl. Acad. Sci. **117**, 4015 (2020).
[17] N. Nadkarni, A. F. Arrieta, C. Chong, D. M. Kochmann, and C. Daraio, Unidirectional Transition Waves in Bistable Lattices, Phys. Rev. Lett. **116**, 244501 (2016).
[18] M. Hwang and A. F. Arrieta, Input-independent energy harvesting in bistable lattices from transition waves, Sci. Rep. **8**, 1 (2018).
[19] N. Kidambi, Y. Zheng, R. L. Harne, and K. W. Wang, in *Proceedings of SPIE 10595, Active and Passive Smart Structures and Integrated Systems XII*, (2018), p. 1059510.
[20] N. Nadkarni, C. Daraio, and D. M. Kochmann, Dynamics of periodic mechanical structures containing bistable elastic elements: From elastic to solitary wave propagation, Phys. Rev. E – Stat. Nonlinear Soft Matter Phys. **90**, 1 (2014).
[21] M. Schaeffer and M. Ruzzene, Wave propagation in multistable magneto-elastic lattices, Int. J. Solids Struct. **56**, 78 (2015).
[22] J. R. Raney, N. Nadkarni, C. Daraio, D. M. Kochmann, J. A. Lewis, and K. Bertoldi, Stable propagation of mechanical signals in soft media using stored elastic energy, Proc. Natl. Acad. Sci. **113**, 9722 (2016).
[23] T. A. M. Hewage, K. L. Alderson, A. Alderson, and F. Scarpa, Double-negative mechanical metamaterials displaying simultaneous negative stiffness and negative Poisson's ratio properties, Adv. Mater. **28**, 10323 (2016).
[24] K. K. Dudek, R. Gatt, M. R. Dudek, and J. N. Grima, Negative and positive stiffness in auxetic magneto-mechanical metamaterials, Proc. R. Soc. A: Math. Phys. Eng. Sci. **474**, 20180003 (2018).
[25] X. Tan, S. Chen, B. Wang, S. Zhu, L. Wu, and Y. Sun, Design, fabrication, and characterization of multistable mechanical metamaterials for trapping energy, Extreme Mech. Lett. **28**, 8 (2019).
[26] C. R. Tipton, E. Han, and T. Mullin, Magneto-elastic buckling of a soft cellular solid, Soft Matter **8**, 6880 (2012).
[27] J. N. Grima, R. Caruana-Gauci, M. R. Dudek, K. W. Wojciechowski, and R. Gatt, Smart metamaterials with tunable auxetic and other properties, Smart Mater. Struct. **22**, 084016 (2013).
[28] A. G. Izard and L. Valdevit, Magnetoelastic metamaterials for energy dissipation and wave filtering, Adv. Eng. Mater. **22**, 1901019 (2019).
[29] B. Deng, P. Wang, V. Tournat, and K. Bertoldi, Nonlinear transition waves in free-standing bistable chains, J. Mech. Phys. Solids **136**, 103661 (2020).
[30] See Supplemental Material at http://link.aps.org/supplemental/10.1103/PhysRevApplied.13.054067 for details on our static and dynamic analysis on rotating squares, prototype fabrication, experiments, and tensile tests on a chain with SDWs.
[31] The geometric phase diagram is analogous to an isothermal section of a ternary phase diagram for classical alloys. The tristable, bistable, and monostable regions of the geometric phase diagram correspond to three-phase, two-phase, and single-phase regions, respectively, of a ternary phase diagram, and the same basic rules are observed in the arrangements of the phase regions (e.g., monostable and bistable regions are found at the vertices and edges, respectively, of the tristable regions).
[32] B. Deng, J. R. Raney, V. Tournat, and K. Bertoldi, Elastic Vector Solitons in Soft Architected Materials, Phys. Rev. Lett. **118**, 204102 (2017).
[33] C. Mo, J. Singh, J. R. Raney, and P. K. Purohit, Cnoidal wave propagation in an elastic metamaterial, Phys. Rev. E **100**, 013001 (2019).
[34] M. Sanati and A. Saxena, Half-kink lattice solution of the $\phi 6$ model, J. Phys. A: Math. Gen. **32**, 4311 (1999).
[35] A. M. Wazwaz, Compactons, solitons and periodic solutions for some forms of nonlinear Klein-Gordon equations, Chaos Solitons Fractals **28**, 1005 (2006).
[36] A. Khare and A. Saxena, Domain wall and periodic solutions of a coupled $\phi 6$ model, J. Math. Phys. **49**, 063301 (2008).
[37] M. Hwang and A. F. Arrieta, in *Proceedings of SPIE 10170, Health Monitoring of Structural and Biological Systems 2017* (2017), p. 101701A.
[38] N. Nadkarni, C. Daraio, R. Abeyaratne, and D. M. Kochmann, Universal energy transport law for dissipative and diffusive phase transitions, Phys. Rev. B **93**, 1 (2016).
[39] B. Deng, V. Tournat, P. Wang, and K. Bertoldi, Anomalous Collisions of Elastic Vector Solitons in Mechanical Metamaterials, Phys. Rev. Lett. **122**, 044101 (2019).
[40] M. Remoissenet, *Waves Called Solitons: Concepts and Experiments* (Springer, Berlin, 1996).
[41] A. Rafsanjani, L. Jin, B. Deng, and K. Bertoldi, Propagation of pop ups in Kirigami shells, Proc. Natl. Acad. Sci. **116**, 8200 (2019).